Journal of Electroanalytical Chemistry 979 (2025) 118906

Contents lists available at ScienceDirect

Journal of Electroanalytical Chemistry

journal homepage: www.elsevier.com/locate/jelechem

Electrochemically synthesized MoS_2 with enhanced S-bonds for hydrogen evolution

Fajun Li [a,b,*], Yuqi Ma [a], Rui Xu [a], Jingyang Chen [c], Shujin Kan [a], Guizhi Wang [a], Haifeng Xu [a], Zhong Jin [a,b,*]

[a] Anhui Key Laboratory of Spin Electron and Nanomaterials, School of Chemistry and Chemical Engineering, Suzhou University, Suzhou 234000, China
[b] MOE Key Laboratory of Mesoscopic Chemistry, MOE Key Laboratory of High Performance Polymer Materials and Technology, Jiangsu Key Laboratory of Advanced Organic Materials, School of Chemistry and Chemical Engineering, Nanjing University, Nanjing 210023, China
[c] School of Metallurgical Engineering, Anhui University of Technology, Maanshan 243032, China

ARTICLE INFO

Keywords:
Chemical bond S_2^{2-}
Water splitting
Hydrogen evolution reaction
Heterojunction structure
Theoretical calculations

ABSTRACT

Low-cost, highly active, and robust electrocatalysts are needed for more efficient H_2 production from water splitting, herein, we present an amorphous MoS_2-Ni_3S_2 heterostructure on the nickel foam (NF) substrate via a facile hydrothermal treatment and a one-step electrodeposition approach. The S_2^{2-} sites in the fabricated electrocatalyst could be conveniently modulated by synthesis conditions. The optimized amorphous MoS_2-Ni_3S_2@NF-24 shows an excellent electrocatalytic activity for HER with the overpotential of 58 mV at 10 mA cm^{-2} and stabilizes for over 50 h when used as a bifunctional catalyst for overall water splitting in 1 M KOH electrolyte at room temperature. Experimental characterizations and DFT calculations demonstrate that the excellent electrocatalytic performance of the fabricated heterostructure could be attributed to the synergistic effect of the proper hydrogen binding free energies of MoS_2 with abundant bridging S_2^{2-} and the strong adsorption of OH^- to the Ni_3S_2. This work proposed a finely designed MoS_2-based hybrid catalyst for efficient alkaline HER, thus providing insights into the design and fabrication of inexpensive electrocatalysts for wide range of applications.

1. Introduction

The environmental and energy crisis is getting worse, and the urgent need for promising alternatives to petroleum fuel is growing [1,2]. It is worth noting that hydrogen, with the highest gravimetric energy and zero-polluting combustion product, can resolve the current problems as well as sustain long-term development [3,4]. In this regard, hydrogen generation technique has become the key factor for the successful realization of hydrogen economy, and an efficient electrolysis of water to produce hydrogen is desirable and also an important semi-reaction for Chlor-alkali industry when compared with steam hydrogen production that consumes fuels and emits CO_2 [5]. In alkaline medium, the water electrolysis reaction process, consisting of the reacting species H_2O molecule and OH^-, involves the adsorption of H_2O molecule and its cleavage of HO—H covalent bonds [6]. Therefore, the catalyst must feature both appropriate catalyst-hydrogen and catalyst-hydroxyl interactions [7,8]. Although Pt and its composites have been known as the "Holy Grail" and state-of-the-art electrocatalysts for hydrogen evolution reaction (HER), the high cost (250 $peroz.) and rareness on Earth remain the major bottlenecks that limit the widespread uses and large-scale commercial applications [9–12]. Consequently, developing non-noble-metal alternatives is always highly attractive [13,14].

Transition metal dichalcogenides (TMDs) have attracted momentous attention in various research fields on account of chemical stability and catalytic activity [15–18]. Of all the materials studied, molybdenum disulfide (MoS_2) has been established as an efficient HER electrocatalyst in alkaline media as a result of the appropriate ΔG_H [19,20]. However, the high-energy barrier for H_2O dissociation is still challenging [21]. Scholars have reported that several characteristics including but not limited edges [22,23], morphology [24], crystallinity [25,26], or vacancy defects of MoS_2 may trigger high-efficiency HER, and although the accurate catalytically active sites are ambiguous, nevertheless, the S_2^{2-}

* Corresponding authors at: Anhui Key Laboratory of Spin Electron and Nanomaterials, School of Chemistry and Chemical Engineering, Suzhou University, Suzhou 234000, China.
E-mail addresses: lifajuncl2012@163.com (F. Li), zhongjin@nju.edu.cn (Z. Jin).

https://doi.org/10.1016/j.jelechem.2024.118906
Received 3 November 2024; Received in revised form 22 December 2024; Accepted 25 December 2024
Available online 28 December 2024

ligands have deeply played a crucial role [27–29]. It is widely acknowledged that the high catalytic HER activity stemmed from the active S sites on the edge can effectively boost the reduction rate of H^+ to H_2 via enriching H^+ from solution [30,31], and an S-rich catalyst obtained via a hydrothermal route has been proved to provide abundant exposed S edges and bridging ligands for interfacial hydrogen evolution [32,33]. In such a heterogeneous structure, one component promotes the adsorption of H_2O and facilitates the cleavage of the HO—H bond while the other component is responsible for the adsorption and desorption of hydrogen, and finally the synergistic effects derived from the heterogeneous interfaces can improve the HER performance. In a word, the fabrication of a heterostructure catalyst with hybridized multiple functional components is an effective strategy to promote the alkaline HER [34–37].

In present, an amorphous MoS_2-Ni_3S_2 heterostructure on Ni foam (MoS_2-Ni_3S_2/NF) was synthesized by means of a facile and low-cost fabrication, via a hydrothermal treatment and a one-step electrodeposition. The composition as well as the bridging S_2^{2-} content of the fabricated heterostructure can be facilely regulated by the hydrothermal treatment time and deposition potential. The fabricated amorphous heterostructure exhibits a high catalytic activity toward the HER in 1 M KOH solution with an overpotential of 58 mV at 10 mA cm^{-2} and an excellent stability over 50 h when used as both OER and HER electrocatalysts. The experimental studies and theoretical calculations demonstrate that such a superior electrocatalytic performance of the MoS_2-Ni_3S_2@NF-24 heterostructure is due to the high content of the bridging S_2^{2-} and the synergistic effect in the heterogeneous structure material.

2. Experimental

2.1. Materials

Hexaammonium heptamolybdate tetrahydrate ($(NH_4)_6Mo_7O_{24}\cdot 4H_2O$, AR), Potassium hydroxide (KOH, AR), and Potassium chloride (KCl, AR) were purchased from Sinopharm Chemical Reagent; Sodium sulfide nonahydrate ($Na_2S\cdot 9H_2O$, AR) was purchased from Aladdin Chemical Reagent; and Thioacetic acid (CH_3COSH, 95 %) was obtained from Adamas-beta Chemical Reagent. Argon (99.9 %) was purchased from Yuyang gas plant, Suzhou. All reagents were used without further purifcation. Ni foam (99.99 %) was purchased from Jiayisheng Electronics Co., Ltd. Ni foam, used as the substrate as well as Ni source, was ultrasonically pretreated in 1.0 M hydrochloric acid, acetone and ethanol to remove the surface oxides. All solutions were prepared using 18.2-MΩ deionized H_2O.

2.2. Hydrothermal treatments

The surface of the Ni foam would be etched by sulfur through a facile one-pot hydrothermal reaction. Firstly, 20 mL thioacetic acid and 50 mL deionized water were well mixed and transferred to the 100 mL Teflon-lined stainless-steel autoclave. Then, a pretreated 1 cm × 7 cm NF, leaning against the inner wall, was fully immersed. Subsequently, the above device was maintained at 120 °C for 6, 12, or 24 h. After cooling to room temperature, the NiS_x/NF (recorded as NiS_x/NF-6, NiS_x/NF-12, and NiS_x/NF-24, respectively, according to the reaction time) were washed with deionized water several times and dried in a vacuum oven at 60 °C overnight.

2.3. Electroplating experiments

The electroplating solution is prepared as follows: 0.027 g $(NH_4)_6Mo_7O_{24}\cdot 4H_2O$, 0.144 g $Na_2S\cdot 9H_2O$ and 1.120 KCl were dissolved into 150 mL deionized water under constant stirring. The target amorphous hybrid was electrodeposited in the electroplating solution with the NiS_x/NF (obtained from Section 2.2) as the working electrode, an Ag/AgCl (sat. KCl) as the reference electrode, and a graphite as the counter electrode.

2.4. Electrochemical measurements

All the electrochemical measurements were performed on a CHI760E electrochemical workstation (Chenhua Instruments). The HER activity was measured in a glass cell filled with a 1.0 M KOH solution under an Ar atmosphere, with MoS_2-NiS_x/NF as the working electrode, an Hg/HgO (1 M KOH) as the reference electrode, and a graphite as the counter electrode. The measured potentials can be converted to a reversible hydrogen electrode (RHE) using the equation: $E_{vs.RHE} = E_{vs.Hg/HgO} + 0.098 + 0.0591 \times pH$.

Linear sweep voltammetry (LSV) was carried out in a potential range of −0.8 to −1.5 V vs. Hg/HgO at a sweep rate of 5 mV s^{-1}. The stable test was recorded at the cell voltage of 1.53 V. The electrochemical impedance spectroscopy (EIS) was determined at an open-circuit potential in the frequency range of 10^5–10^{-2} Hz with an amplitude of 5 mV. The electrochemical double-layer capacitance C_{dl} of the catalyst sample was evaluated based on the CV curves in a non-Faradaic potential window at scan rates of 10, 20, 30, 40, 50 mV s^{-1}. The electrochemically active surface area (ECSA) can be calculated by the equation with C_s value of 40 μF cm^{-2}: $ECSA = (C_{dl}/C_s) \times A$ [38,39].

2.5. Characterization

Scanning electron microscopy (SEM) imaging was carried out on a FEI Magellan 400 extreme high resolution (XHR) SEM scanning electron microscope. Raman spectra were collected on an in Via Renishaw Raman spectrometer system using a green laser. High-Resolution Transmission Electron Microscopy (HRTEM) imaging was carried out on a JEOL JEM2100F analytical TEM operating at 200 kV.

2.6. Calculation specification

Periodic plane-wave density functional theory (DFT) calculations were performed using the Vienna ab initio simulation package (VASP) [40]. The exchange–correlation was described by the Perdew-Burke-Ernzerhof revised for solids (PBE) method of the generalized gradient approximation (GGA) with a plane-wave kinetic cutoff energy of 450 eV [41]. The projector augmented wave (PAW) depicted non-spherical contributions to the core from the gradient corrections [42]. The long-range interaction was characterized by the DFT-D3 method of Grimme with zero dampings [43]. The Brillouin zone was surface sampled by the Monkhorst–Pack grid with a 3 × 3 × 1 k points mesh for Mxenes supercells geometrical relaxation. The convergence threshold was set to be 1×10^{-4} eV for energy and 0.02 eV/A for force. In order to avoid the interactions, 2 × 2 supercells of Ni_3S_2, MoS_2 monolayers and their heterojunction structure with a vacuum layer of 15 Å were created.

3. Results and discussion

The fabrication proceeds were carried out through a hydrothermal treatment and a one-step electrodeposition. The pretreated NF with flaky texture (as shown in Fig. S1) was immersed in a thioacetic acid aqueous solution and reacted in an autoclave at 120 °C for a period of time. Fig. 1a displays that a rough and granular surface was obtained after 6 h of hydrothermal reaction, and then the grains on the surface gradually became compact (Fig. 1b) and even smooth (Fig. 1c) with time. It can be seen that the surface, accompanying with dense granular, compact granular or smooth structure, has undergone a significant change compared with the bare NF which exhibits a scaly surface. Furthermore, the EDS spectra presented in Fig. S2 indicate that the deposition time can effectively regulate the sulfur bond content.

Subsequently, electroplating investigations of MoS_2 were conducted,

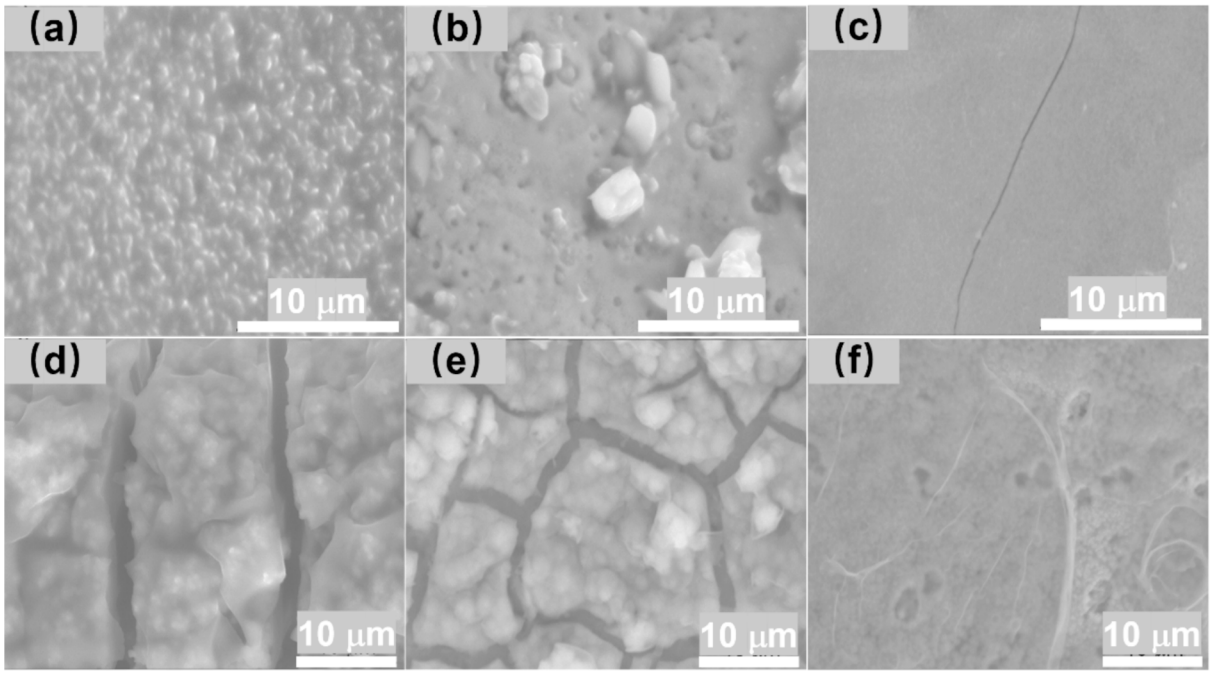

Fig. 1. SEM images of the hydrothermal reactions in thioacetic acid for (a) 6 h, (b) 12 h, (c) 24 h, and corresponding images of MoS_2 electroplated on them (d, e, f).

and firstly, the electrodeposition on NF was studied by CV, as shown in Fig. S3, with a cathodic peak at around −0.8 V (vs. Ag/AgCl), which was responsible for the electrochemical reduction of $Mo_7O_{24}^{6-}$ [44]. The reaction process speculated were as follows:

$$Mo_7O_{24}^{6-} + 14e^- + 10H_2O \rightarrow 7MoO_2 + 20OH^- \quad (1)$$

$$MoO_2 + 2S^{2-} + 2H_2O \rightarrow MoS_2 + 4OH^- \quad (2)$$

$$Mo_7O_{24}^{6-} + 14S^{2-} + 24H_2O + 14e^- \rightarrow 7MoS_2 + 48OH^- \quad (3)$$

Meanwhile, the SEM image (Fig. S4a) shows that the layer electrodeposited on NF for 20 min was a uniform granular film with some cracks, and in addition, the layer curled up if electroplating was continued (Fig. S4b, 4c). The mapping analysis of samples (Fig. S5) exhibit that Mo, S and Ni elements were mainly distributed in the upper layer, in the meantime, the Ni signal predominantly came from the NF substrate and the layer, which was stronger in the crack area but significantly attenuated in the area covered by the upper layer. Therefore, the samples after hydrothermal reaction were electroplated for 20 min so that the thicker granular films could be obtained (Fig. 1d, e), and interestingly, a dense granular film without cracks was attained (Fig. 1f), which was attributed to the smooth surface achieved by the 24 h hydrothermal reaction. The mapping images in Fig. S6 also show a more uniform distribution of Mo, S and Ni elements on the surface without cracks.

Fig. 2a illustrates that the XRD patterns of these samples displayed characteristic nickel diffraction peaks at 44.37° and 51.59° (JCPDS #01-1258), attributed to the nickel foam (NF) substrate. Additionally, the NF subjected to hydrothermal reactions in thioacetic acid revealed diffraction peaks at 21.76°, 31.10°, 37.80°, 49.72° and 54.62°, corresponding to Ni_3S_2 (JCPDS #30-0863). In contrast, the electrodeposited samples demonstrated obvious reflections at 14.39°, indicative of MoS_2 species (JCPDS #06-0097), alongside the Ni_3S_2 signals. Otherwise, the diffraction peak observed at 64.48° corresponding to Ni_3S_4 (JCPDS #08-0106) may be attributed to the substantial presence of sulfur bonds on the substrate surface following the hydrothermal reaction. Furthermore, the subsequent plating experiments were likely to deplete these chemical bonds. Therefore, the HRTEM image of NiS_x/NF-24 (Fig. 2b) exhibits lattice fringes of 0.41 and 0.14 nm, corresponding to the d-spacings of Ni_3S_2 (1 0 1) and Ni_3S_4 (5 3 3), which were also consistent with the XRD diffraction peaks at 21.76° and 64.48° in Fig. 2a. In addition, the HRTEM image of MoS_2-NF (Fig. 2c) shows another lattice fringe of 0.62 nm, corresponding to the d-spacing of MoS_2 (0 0 2), which was consistent with the broad XRD diffraction peak around14.40° in Fig. 2a. Moreover, the HRTEM image of MoS_2-Ni_3S_2/NF-24 (Fig. 2d) displays four different lattice fringes, in addition to those already known, the other two lattice fringes with the d-spacings of 0.24 and 0.29 nm were related to the (0 0 3) and (1 1 0) planes of the Ni_3S_2 layer, in according with the broad XRD diffraction peak 37.80° and 31.10°. This is attributable to the fact that the electroplating reaction consumes a portion of the surface sulfur bonds, which can also be proved from reaction Eq. (3). The XPS characterization (Fig. 2e) indicates that the peaks at 872.98 eV and 855.18 eV corresponded to the Ni $2p_{1/2}$ and Ni $2p_{3/2}$ orbitals of Ni^{2+}, while the peaks at 875.18 eV and 857.48 eV corresponded to the Ni $2p_{1/2}$ and Ni $2p_{3/2}$ orbitals of Ni^{3+}, respectively [45]. The peaks observed at 228.6 eV, 231.4 eV, and 232.4 eV were associated with the Mo $3d_{5/2}$ orbitals of Mo^{4+}, Mo^{5+}, and Mo^{6+}, respectively. Furthermore, the peak at 226.1 eV in the Mo 3D spectrum was attributed to the S 2 s peak [46]. The peaks observed at 161.9 eV and 163.2 eV were attributed to terminal S^{2-} and bridging S_2^{2-}, respectively. Furthermore, an additional peak at 168.6 eV was associated with the S—O bond [47].

The polarization curves were measured in 1 M KOH at room temperature as shown in Fig. 3a, it can be seen that the HER overpotential on the bare NF substrate was about 251 mV at 10 mA cm^{-2}. The MoS_2-Ni_3S_2@NF-24 exhibits a lower HER overpotential of 58 mV at 10 mA cm^{-2} compared to the MoS_2-NF (η_{10} = 90 mV), NiS_x/NF-24 (η_{10} = 195 mV), indicating that the MoS_2-Ni_3S_2@NF-24 hybrid has a better HER catalytic activity. The Tafel analysis was performed to evaluate the kinetics as well as to clarify the rate-determining step (RDS) of the HER. The MoS_2-Ni_3S_2@NF-24 renders a HER Tafel slope of around 47.5 mV dec^{-1} (Fig. 3b), which is smaller than that on the bare NF substrate (181.8 mV dec^{-1}), NiS_x/NF-24 (107.4 mV dec^{-1}), and MoS_2-NF (72.1 mV dec^{-1}), suggesting a Volmer-Heyrovsky mechanism and facile kinetics for the HER on the fabricated MoS_2-Ni_3S_2@NF-24 due to the support of Ni_3S_2 and NF on the improved adsorption of OH^- and H_2O, respectively. It is worth noticing that although the MoS_2-Ni_3S_2 is grown

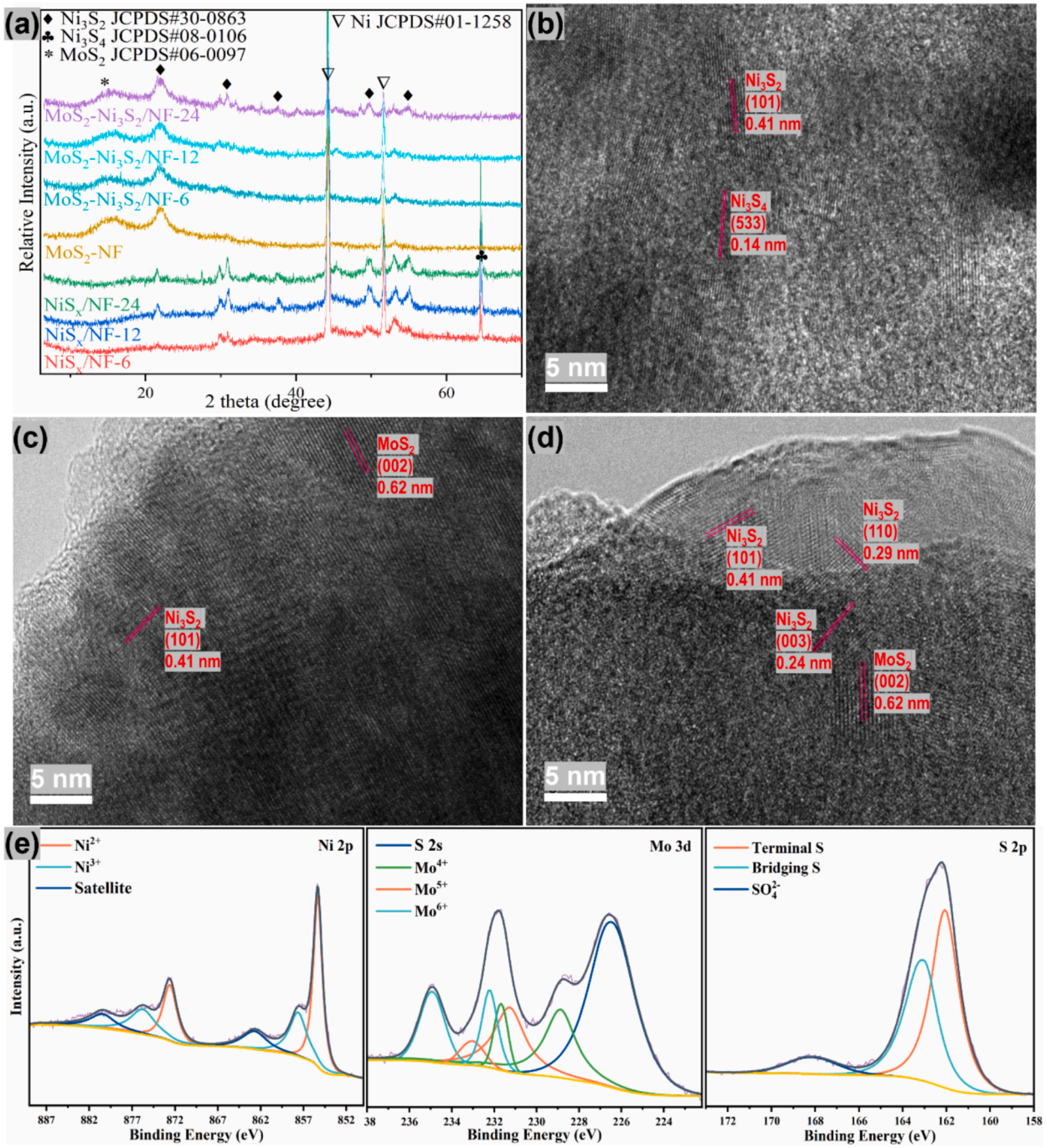

Fig. 2. (a) XRD patterns of the samples; HRTEM images of (b) NiS_x/NF-24, (c) MoS_2-NF, (d) MoS_2-Ni_3S_2/NF-24; and (e) XPS spectra of Ni 2p, Mo 3d, S 2p of the MoS_2-Ni_3S_2/NF-24.

on top of the NF, it has shared chemical bonds and possibly capillaries between the grains (Fig. 1f), through which the electrolyte could infiltrate to reach the interfaces. Moreover, EIS in Fig. S7 and equivalent electric circuit inset were conducted to estimate the catalytic kinetics of the HER on these samples, where the R_s, R_c and R_{ct} represented the bulk solution resistance, contact resistance, and the charge-transfer resistance at the electrode/electrolyte interface, respectively. As shown in Table S1, the MoS_2-Ni_3S_2@NF-24 exhibits the smallest R_{ct} of 0.03 Ω at the open-circuit potential, which is lower than the R_{ct} values obtained on the bare NF substrate (3.17 Ω), NiS_x/NF-24 (0.11 Ω) and MoS_2-NF (0.09 Ω). Besides, the MoS_2-Ni_3S_2@NF-24 also owns the smallest R_c (Table S1). These results indicate that the MoS_2-Ni_3S_2@NF-24 owns a low barrier of charge transfer, which is beneficial for the excellent catalytic performance as an electrocatalyst for the HER. It can also be seen from Fig. 3c that the overpotential increases accordingly with the increasing current, however MoS_2-Ni_3S_2@NF-24 still shows the best performance. For deep insight into the synergistic effect of the hetero-interface, density functional theory (DFT) calculations were performed to reveal the local charge density difference and adsorption/desorption energy of reactive intermediates. Fig. S8 display the optimized S-exposed, Ni-exposed sections and H adsorption of Ni_3S_2 (1 1 0) (1 0 1); and the optimized heterogeneous structure of MoS_2-Ni_3S_2 (1 1 0) and H adsorption. Fig. 3d shows that Ni_3S_2 or MoS_2 can act as additional water dissociation sites for HER under alkaline conditions, which are similar to previous reports [48], and consistent with the results of Fig. 3a. It can be speculated that there are charge concentration enhanced and decreased

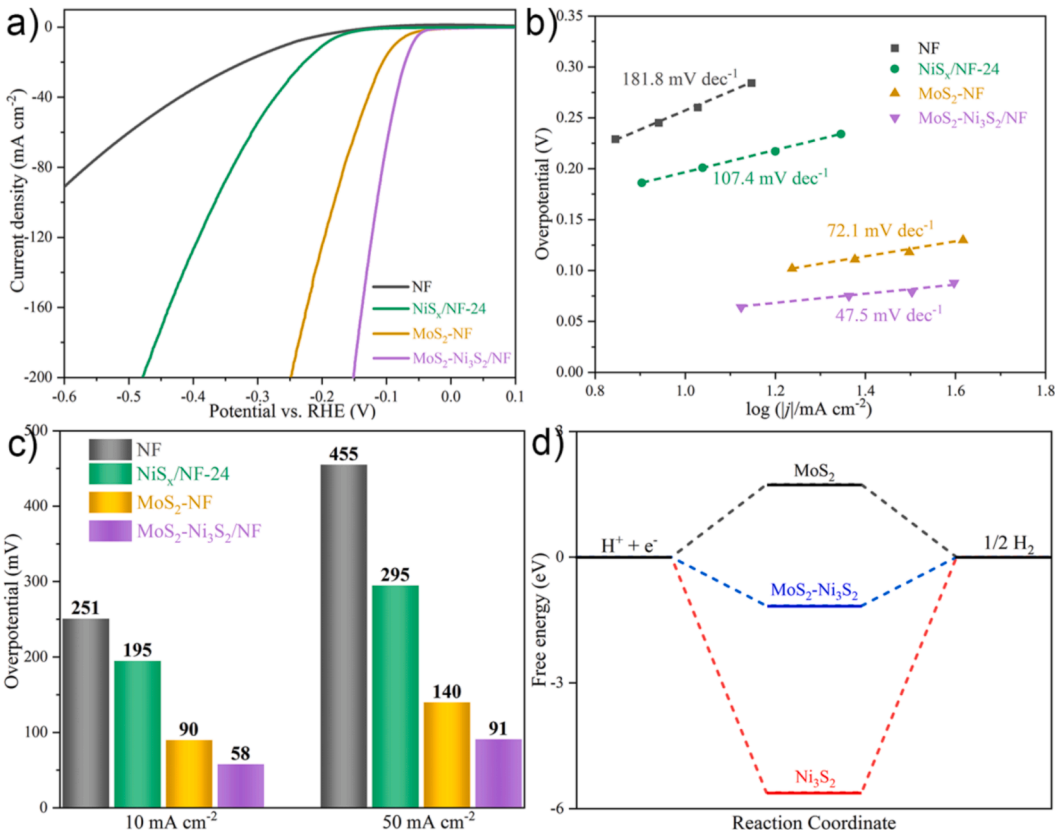

Fig. 3. (a) Polarization curves and (b) The corresponding steady-state HER Tafel plots of the fabricated samples, (c) HER overpotentials at 10 and 50 mA cm^{-2}, (d) Calculated free energy for atomic hydrogen adsorption on the as-prepared samples.

areas around the MoS_2-Ni_3S_2 interface. Both experiment results and calculation results prove the existence of electron interaction between MoS_2 and Ni_3S_2, and the electronic structure on the interface has been adjusted. The free energy diagram of the water dissociation process contains three steps: H_2O adsorption, transition state, and final state. Crucially, H—OH bond is cleaved and the H* intermediates are caught by S atoms of Ni_3S_2. Then, H* intermediates transfer to S atoms of MoS_2 spontaneously. As the MoS_2-Ni_3S_2/NF-24 displayed the lowest faradaic impedance of the prepared samples (Fig. S7), the resulting facile electron transfer between the substrate and heterojunction composite with abundant catalytic edges sites facilitated the kinetics for HER [49]. The initial adsorption of the proton to form adsorbed hydrogen (Volmer) is generally considered to be fast, while the subsequent hydrogen desorption step (either Heyrovsky or Tafel) is typically rate limiting [24]. In this sense, it is clear that the binding energy of the adsorbed hydrogen intermediate is crucial, i.e., an optimum state is necessary so that the intermediate is neither too tightly (desorption-limited) nor too loosely (adsorption-limited) bound. As shown in Fig. 3d, the enhanced S bond in MoS_2-Ni_3S_2 displays the optimal ΔG_H* (−1.15 eV) compared to the S site in MoS_2 (1.73 eV), S site in Ni_3S_2 (−5.62 eV), therefore, the finely designed MoS_2-Ni_3S_2 interfaces with the tailored electronic structure are beneficial for the highly efficient HER catalysis, MoS_2-Ni_3S_2/NF-24 has advantages over both Ni_3S_2 and MoS_2.

The MoS_2-Ni_3S_2@NF-24 has the best catalytic activity toward the HER among all the prepared samples in this work. In order to investigate the effect of differences in the surface morphology of the prepared samples on their HER activity, the electrochemically active surface area (ECSA) of each catalyst were estimated by determining the double-layer capacitance of the system from CV. A non-Faradaic potential range was identified from CV (Fig. S9) in quiescent solution, and all measured current in this region was assumed to be due to double-layer charging. Based on this assumption, the charging current, i_c, is equal to the product of the electrochemical double layer capacitance, C_{dl}, and the scan rate, ν, as shown $i = \nu\, C_{dl}$. And then i_c was plotted as a function of ν, yielding a straight line with slope equal to C_{dl}. The ECSA of the catalyst can be calculated by dividing C_{dl} by the specific capacitance of the sample as shown ECSA = C_{dl}/C_s (Fig. 4a). It can be seen that ECSA of MoS_2-Ni_3S_2@NF-24 is much higher than that of other electrocatalysts. It therefore appears that in general MoS_2-Ni_3S_2@NF-24 gives a higher specific surface area and an amorphous structure is favored for electrocatalytic performance due to the existence of the S-rich bonding that serves as active site. The MoS_2-Ni_3S_2@NF-24 was further evaluated as a bifunctional catalyst for overall water splitting. A full-cell water splitting with two identical electrodes was tested (inset in Fig. 4b). The LSV curves (Fig. 4b) show that the MoS_2-Ni_3S_2@NF-24 full cell affords a current density of 10 and 50 mA cm^{-2} at cell voltages of 1.28 and 1.53 V, respectively. The long-term durability test (Fig. 4c) shows the superior durability of over 50 h at the cell voltage of 1.53 V. Furthermore, it can be seen from the inset in the Fig. 4c that the material structure and morphology can also be maintained well. In addition, LSV curves for HER were performed before and after 50 h of electrolysis to examine the stability of the MoS_2-Ni_3S_2@NF-24 as electrocatalyst as shown in Fig. 4d, and the curves of LSV and XRD inset show negligible decay, proving a promising catalyst.

4. Conclusion

In summary, an amorphous MoS_2-Ni_3S_2 heterostructure is rationally designed and successfully fabricated on the NF substrate via a facile hydrothermal treatment and a one-step electrodeposition approach as an electrocatalyst for the HER in alkaline solutions. The advantages of this fabricated heterostructure are clarified by experimental characterizations and theoretical calculations. Consequently, the MoS_2 with abundant bridging S_2^{2-} provides high-active sites for the adsorption/

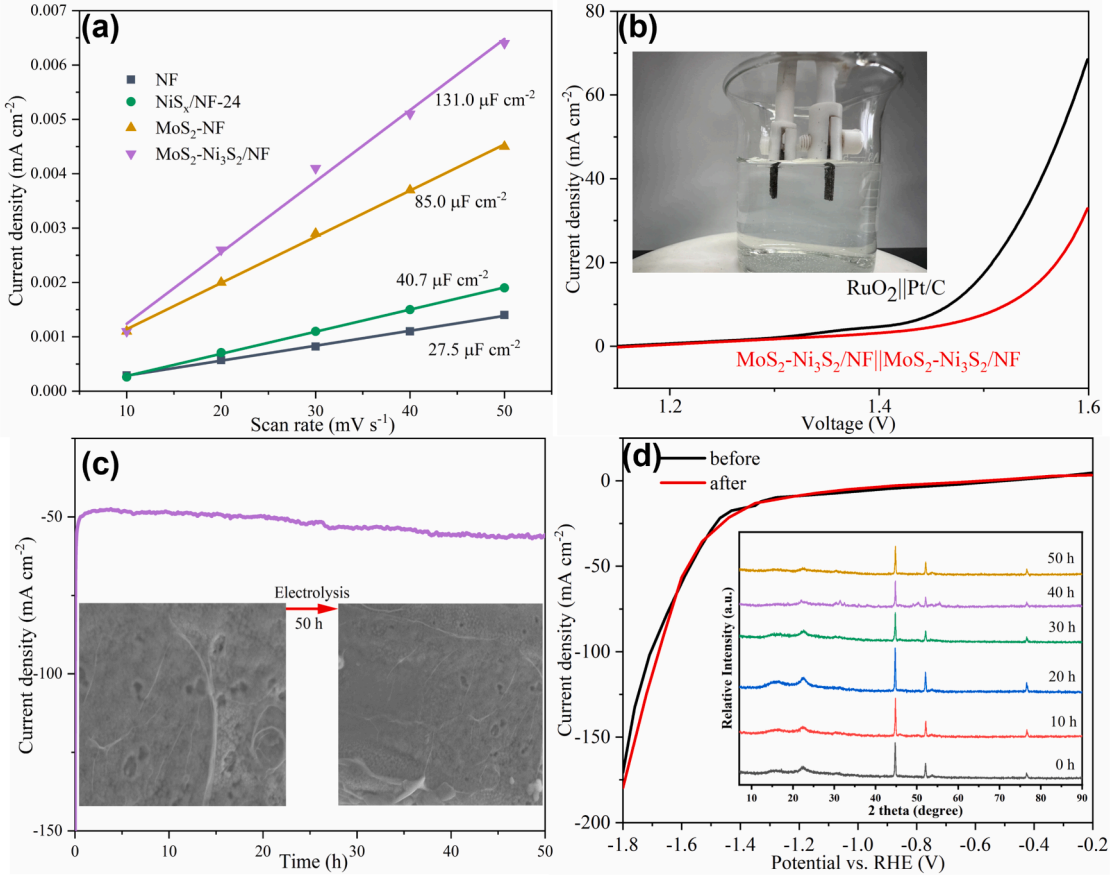

Fig. 4. (a) The resulting C_{dl} plots, (b) Overall water splitting in 1 M KOH of RuO_2||Pt/C and MoS_2-Ni_3S_2/NF||MoS_2-Ni_3S_2/NF as OER and HER electrocatalyst, (c) Durability test at the cell voltage of 1.53 V, (d) Stability test of MoS_2-Ni_3S_2/NF before and after 50 h electrolysis.

desorption of the H* intermediate and Ni_3S_2 improves the adsorption of OH^- during the HER. Due to the synergistic effect, the optimized amorphous MoS_2-Ni_3S_2@NF-24, prepared at hydrothermal 120 °C for 24 h followed by electrodeposition for 20 min, achieves an overpotential of 58 mV to drive the alkaline HER at 10 mA cm^{-2} and could be stable for over 50 h when used as a bifunctional catalyst for overall water splitting. This work indicates that the electrocatalytic activity of MoS_2 for alkaline HER can be boosted by co-operating with other catalysts as well as by increasing the bridging S_2^{2-}. This strategy can also be employed to design and fabricate other MoS_2-based catalysts for different applications.

CRediT authorship contribution statement

Fajun Li: Writing – original draft. **Yuqi Ma:** Data curation. **Rui Xu:** Formal analysis. **Jingyang Chen:** Software. **Shujin Kan:** Software. **Guizhi Wang:** Investigation. **Haifeng Xu:** Methodology. **Zhong Jin:** Project administration.

Declaration of competing interest

The authors declare that they have no known competing financial interests or personal relationships that could have appeared to influence the work reported in this paper.

Acknowledgments

This work was supported by the National Natural Science Foundation of China (22206145), the Provincial of Natural Science Foundation of Anhui (2208085QB65), the Excellent Youth Research Project of Anhui Province (2023AH030100), and the Natural Science Research Project and Quality Engineering Projects of Anhui Provincial Education Department (2022AH040209, 2022zybj094, 2023yzd16), the Scientific Research Platform (2021XJPT07) and the Doctoral Research Foundation (2021BSK011) of Suzhou University, and the Specialized Services for the Top Ten Emerging Industries in Anhui Province (szxy2022fwxxcy01). This work was also supported by Anhui Province Young Backbone Teachers' In-country Study Visit Programme (JNFX2023067).

Appendix A. Supplementary material

Supplementary data to this article can be found online at https://doi.org/10.1016/j.jelechem.2024.118906.

References

[1] M. Yao, B. Wang, B. Sun, L. Luo, Y. Chen, J. Wang, N. Wang, S. Komarneni, X. Niu, W. Hu, Rational design of self-supported Cu@WC core-shell mesoporous nanowires for pH-universal hydrogen evolution reaction, Appl. Catal. B 280 (2021) 119451.
[2] X. Zhao, K. Tang, X. Wang, W. Qi, H. Yu, C.-F. Du, Q. Ye, A self-supported bifunctional $MoNi_4$ framework with iron doping for ultra-efficient water splitting, J. Mater. Chem. A 11 (2023) 3408–3417.
[3] B. You, M.T. Tang, C. Tsai, F. Abild-Pedersen, X. Zheng, H. Li, Enhancing electrocatalytic water splitting by strain engineering, Adv. Mater. 31 (17) (2019) 1807001.
[4] Y. Zhang, Z. Li, L. Hou, X. Liu, Thermal shrinkage engineering enables electrocatalysts for stable hydrogen evolution at 2000 mA cm^{-2}, Adv. Funct. Mater. 33 (16) (2023) 2213976.
[5] J. Zhu, L. Hu, P. Zhao, L.Y.S. Lee, K.Y. Wong, Recent advances in electrocatalytic hydrogen evolution using nanoparticles, Chem. Rev. 120 (2) (2020) 851–918.
[6] P. Wang, X. Zhang, J. Zhang, S. Wan, S. Guo, G. Lu, J. Yao, X. Huang, Precise tuning in platinum-nickel/nickel sulfide interface nanowires for synergistic hydrogen evolution catalysis, Nat. Commun. 8 (2017) 14580.
[7] J. Zhang, T. Wang, D. Pohl, B. Rellinghaus, R. Dong, S. Liu, X. Zhuang, X. Feng, Interface engineering of MoS_2/Ni_3S_2 heterostructures for highly enhanced

electrochemical overall-water-splitting activity, Angew. Chem. Int. Ed. Engl. 128 (23) (2016) 6814–6819 {Luo, 2022 #374}.
[8] E. Zhang, W. Song, Review—self-supporting electrocatalysts for HER in alkaline water electrolysis, J. Electrochem. Soc. 171 (5) (2024) 052503.
[9] Y. Wu, F. Li, W. Chen, Q. Xiang, Y. Ma, H. Zhu, P. Tao, C. Song, W. Shang, T. Deng, et al., Coupling interface constructions of $MoS_2/Fe_5Ni_4S_8$ heterostructures for efficient electrochemical water splitting, Adv. Mater. 30 (38) (2018) 1803151.
[10] Y. Zhu, L. Zhang, X. Zhang, Z. Li, M. Zha, M. Li, G. Hu, Double functionalization strategy toward Co-Fe-P hollow nanocubes for highly efficient overall water splitting with ultra-low cell voltage, Chem. Eng. J. 405 (2021) 127002.
[11] V. Jose, V.-H. Do, P. Prabhu, C.-K. Peng, S.-Y. Chen, Y. Zhou, Y.-G. Lin, J.-M. Lee, Activating amorphous Ru metallenes through co integration for enhanced water electrolysis, Adv. Funct. Mater. 13 (2023) 2301119.
[12] P. Prabhu, V.-H. Do, C.-K. Peng, H. Hu, S.-Y. Chen, J.-H. Choi, Y.-G. Lin, J.-M. Lee, Oxygen-bridged stabilization of single atomic W on Rh metallenes for robust and efficient pH-universal hydrogen evolution, ACS Nano 17 (2023) 10733–10747.
[13] Y. Liu, X. Li, Q. Zhang, W. Li, Y. Xie, H. Liu, L. Shang, Z. Liu, Z. Chen, L. Gu, et al., A general route to prepare low-ruthenium-content bimetallic electrocatalysts for pH-universal hydrogen evolution reaction by using carbon quantum dots, Angew. Chem. Int. Ed. Engl. 59 (4) (2020) 1718–1726.
[14] K. Feng, R. Song, J. Xu, Y. Chen, C. Lu, Y. Li, W. Hofer, H. Lin, Z. Kang, J. Zhong, The S-Fe(Ni) sub-surface active sites for efficient and stable overall water splitting, Appl. Catal. B 325 (2023) 122365.
[15] J. Lee, C. Kim, K. Choi, J. Seo, Y. Choi, W. Choi, Y.-M. Kim, H.Y. Jeong, J.H. Lee, G. Kim, et al., In-situ coalesced vacancies on $MoSe_2$ mimicking noble metal: unprecedented Tafel reaction in hydrogen evolution, Nano Energy 63 (2019) 103846.
[16] F. Sun, X. Tian, J. Zang, R. Zhu, Z. Hou, Y. Zheng, Y. Wang, L. Dong, Constructing composite active centers optimized with Cr-doped NiS/NiS_2 heterostructure for efficiently catalyzing alkaline hydrogen evolution reaction, Fuel 363 (2024) 130999.
[17] P. Prabhu, V. Jose, J.-M. Lee, Design strategies for development of TMD-based heterostructures in electrochemical energy systems, Matter 2 (2020) 526–553.
[18] H.T. Bui, N.D. Lam, D.C. Linh, N.T. Mai, H. Chang, S.-H. Han, V.T.K. Oanh, A. T. Pham, S.A. Patil, N.T. Tung, N.K. Shrestha, Escalating catalytic activity for hydrogen evolution reaction on $MoSe_2$@graphene functionalization, Nanomaterials 13 (14) (2023) 2139.
[19] L. Chen, Y. Song, Y. Liu, L. Xu, J. Qin, Y. Lei, Y. Tang, NiCoP nanoleaves array for electrocatalytic alkaline H_2 evolution and overall water splitting, J. Energy Chem. 50 (2020) 395–401.
[20] S. Li, S. Wang, M.M. Salamone, A.W. Robertson, S. Nayak, H. Kim, S.C.E. Tsang, M. Pasta, J.H. Warner, Edge-enriched 2D MoS_2 thin films grown by chemical vapor deposition for enhanced catalytic performance, ACS Catal. 7 (1) (2016) 877–886.
[21] L. Zhang, Y. Zheng, J. Wang, Y. Geng, B. Zhang, J. He, J. Xue, T. Frauenheim, M. Li, Ni/Mo bimetallic-oxide-derived heterointerface-rich sulfide nanosheets with co-doping for efficient alkaline hydrogen evolution by boosting Volmer reaction, Small 17 (10) (2021) 2006730.
[22] B. Hinnemann, P.G. Moses, J. Bonde, K.P. Jorgensen, J.H. Nielsen, S. Horch, I. Chorkendorff, J.K. Norskov, Biomimetic hydrogen evolution: MoS_2 nanoparticles as catalyst for hydrogen evolution, J. Am. Chem. Soc. 127 (15) (2005) 5308–5309.
[23] Y. Yang, H. Fei, G. Ruan, C. Xiang, J.M. Tour, Edge-oriented MoS_2 nanoporous films as flexible electrodes for hydrogen evolution reactions and supercapacitor devices, Adv. Mater. 26 (48) (2014) 8163–8168.
[24] X. Bian, J. Zhu, L. Liao, M.D. Scanlon, P. Ge, C. Ji, H.H. Girault, B. Liu, Nanocomposite of MoS_2 on ordered mesoporous carbon nanospheres: a highly active catalyst for electrochemical hydrogen evolution, Electrochem. Commun. 22 (2012) 128–132.
[25] J. Xie, H. Zhang, S. Li, R. Wang, X. Sun, M. Zhou, J. Zhou, X.W.D. Lou, Y. Xie, Defect-rich MoS_2 ultrathin nanosheets with additional active edge sites for enhanced electrocatalytic hydrogen evolution, Adv. Mater. 25 (40) (2013) 5807–5813.
[26] T. Yang, Y.L. Zhao, Y. Tong, Z.B. Jiao, J. Wei, J.X. Cai, X.D. Han, D. Chen, A. Hu, J. J. Kai, K. Lu, Y. Liu, C.T. Liu, Multicomponent intermetallic nanoparticles and superb mechanical behaviors of complex alloys, Science 362 (6417) (2018) 933–937.
[27] B. Lassalle-Kaiser, D. Merki, H. Vrubel, S. Gul, V.K. Yachandra, X. Hu, J. Yano, Evidence from in situ X-ray absorption spectroscopy for the involvement of terminal disulfide in the reduction of protons by an amorphous molybdenum sulfide electrocatalyst, J. Am. Chem. Soc. 137 (1) (2015) 314–321.
[28] P.D. Tran, T.V. Tran, M. Orio, S. Torelli, Q.D. Truong, K. Nayuki, Y. Sasaki, S. Y. Chiam, R. Yi, I. Honma, et al., Coordination polymer structure and revisited hydrogen evolution catalytic mechanism for amorphous molybdenum sulfide, Nat. Mater. 15 (6) (2016) 640–646.
[29] Y. Liu, S. Jiang, S. Li, L. Zhou, Z. Li, J. Li, M. Shao, Interface engineering of (Ni, Fe) S_2@MoS_2 heterostructures for synergetic electrochemical water splitting, Appl. Catal. B 247 (2019) 107–114.
[30] H. Yu, W. Liu, X. Wang, F. Wang, Promoting the interfacial H_2-evolution reaction of metallic Ag by Ag_2S cocatalyst: a case study of TiO_2/Ag-Ag_2S photocatalyst, Appl. Catal. B 225 (2018) 415–423.
[31] W. Zhong, X. Wu, Y. Liu, X. Wang, J. Fan, H. Yu, Simultaneous realization of sulfur-rich surface and amorphous nanocluster of NiS_{1+} cocatalyst for efficient photocatalytic H_2 evolution, Appl. Catal. B 280 (2021) 119455.
[32] C. Wang, T. Wang, J. Liu, Y. Zhou, D. Yu, J.-K. Cheng, F. Han, Q. Li, J. Chen, Y. Huang, Facile synthesis of silk-cocoon S-rich cobalt polysulfide as an efficient catalyst for the hydrogen evolution reaction, Energ. Environ. Sci. 11 (9) (2018) 2467–2475.
[33] Y. Liu, X. Zhou, Y. Zhou, G. Chen, Construction of Ag decorated 2D rGO/SnS_2 nanostructure towards synergistically enabling overall water splitting, Chem. Eng. J. 433 (2022) 133198.
[34] J. Wei, M. Zhou, A. Long, Y. Xue, H. Liao, C. Wei, Z.J. Xu, Heterostructured electrocatalysts for hydrogen evolution reaction under alkaline conditions, Nanomicro Lett. 10 (4) (2018) 75.
[35] J. Jiang, Y. Wang, J. Wu, H. Wang, Arramel, Y. Zou, J. Zou, H. Wang, Charge transfer interfaces across black phosphorus/Co, N Co-doped carbon heterojunction for enhanced electrocatalytic water splitting, J. Mater. Sci. Technol. 178 (2024) 171–178.
[36] Y. Fan, Y. Yu, D. Sun, Y. Qu, L. Huang, X. Wei, Q. Su, G. Du, B. Xu, K. Wang, Three-dimensional self-supporting micro-nanostructured MoS_2/CoS_2/CC heterojunction derived from ZIF-67 for high efficiency electrocatalytic hydrogen evolution in both acid and alkali electrolytes, J. Alloys Compd. 976 (5) (2024) 173354.
[37] S. Chen, T. Zhang, J. Han, H. Qi, S. Jiao, C. Hou, J. Guan, Interface engineering of Fe-Sn-Co sulfide/oxyhydroxide heterostructural electrocatalyst for synergistic water splitting, Nano Res. Energy 3 (2) (2024).
[38] C.C. McCrory, S. Jung, I.M. Ferrer, S.M. Chatman, J.C. Peters, T.F. Jaramillo, Benchmarking hydrogen evolving reaction and oxygen evolving reaction electrocatalysts for solar water splitting devices, J. Am. Chem. Soc. 137 (13) (2015) 4347–4357.
[39] W. Chen, J. Gu, Y. Du, F. Song, F. Bu, J. Li, Y. Yuan, R. Luo, Q. Liu, D. Zhang, Achieving rich and active alkaline hydrogen evolution heterostructures via interface engineering on 2D 1T-MoS_2 quantum sheets, Adv. Funct. Mater. 30 (25) (2020) 2000551.
[40] T. Bucko, J. Hafner, S. Lebegue, J.G. Angyán, Improved description of the structure of molecular and layered crystals: ab initio DFT calculations with van Der Waals corrections, Chem. A Eur. J. 114 (43) (2010) 11814–11824.
[41] B. Hammer, L.B. Hansen, J.K. Nørskov, Improved adsorption energetics within density-functional theory using revised Perdew-Burke-Ernzerhof functionals, Phys. Rev. B 59 (11) (1999) 7413.
[42] G. Kresse, D. Joubert, From ultrasoft pseudopotentials to the projector augmented-wave method, Phys. Rev. B 59 (3) (1999) 1758.
[43] S. Grimme, S. Ehrlich, L. Goerigk, Effect of the damping function in dispersion corrected density functional theory, J. Comput. Chem. 32 (7) (2011) 1456–1465.
[44] H.-Z. Cao, C.-J. Tong, H.-B. Zhang, G.-Q. Zheng, Mechanism of MoO_2 electrodeposition from ammonium molybdate solution, Trans. Nonferrous Met. Soc. Chin. 29 (8) (2019) 1744–1752.
[45] H. Gao, J. Zang, Y. Wang, S. Zhou, P. Tian, S. Song, X. Tian, W. Li, One-step preparation of cobalt-doped NiS@MoS_2 core-shell nanorods as bifunctional electrocatalyst for overall water splitting, Electrochim. Acta 377 (2021) 138051.
[46] C.-H. Lee, S. Lee, G.-S. Kang, Y.-K. Lee, G.G. Park, D.C. Lee, H.-I. Joh, Insight into the superior activity of bridging sulfur-rich amorphous molybdenum sulfide for electrochemical hydrogen evolution reaction, Appl. Catal. B 258 (2019) 117995.
[47] J.D. Benck, Z. Chen, L.Y. Kuritzky, A.J. Forman, T.F. Jaramillo, Amorphous molybdenum sulfide catalysts for electrochemical hydrogen production: insights into the origin of their catalytic activity, ACS Catal. 2 (9) (2012) 1916–1923.
[48] P. Wang, X. Zhang, J. Zhang, S. Wan, S. Guo, G. Lu, J. Yao, X. Huang, Precise tuning in platinum-nickel/nickel sulfide interface nanowires for synergistic hydrogen evolution catalysis, Nat. Commun. 8 (1) (2017) 14580.
[49] M. Luo, S. Liu, W. Zhu, G. Ye, J. Wang, Z. He, An electrodeposited MoS_2-MoO_{3-x}/Ni_3S_2 heterostructure electrocatalyst for efficient alkaline hydrogen evolution, Chem. Eng. J. 428 (2022) 131055.